



A binder-free high silicon content flexible anode for Li-ion batteries†

Cite this: DOI: 10.1039/c9ee02615k

Hanwei Wang,^{‡a} Jinzhou Fu,^{‡b} Chao Wang,^a Jiangyan Wang,^c Ankun Yang,^c Caicai Li,^{id a} Qingfeng Sun,^{id *a} Yi Cui^{*c} and Huiqiao Li^{id *b}

Despite the high theoretical capacity of Si anodes, their huge volume change and poor electrical connectivity must be overcome by decreasing the feature sizes of the Si particles to the nanoscale and compositing them with highly conductive carbon materials. To ensure the mechanical integrity of the electrodes with uniform dispersion and good electrical contact of the nano-silicon, the industry has to use a relatively low amount of Si (<15% by mass) in commercial anodes. Such a low Si content severely weakens the capacity advantage of silicon at the electrode level. Here, we designed a cellulose-based topological microscroll by the self-rolling of cellulose nanosheets to form a binder-free, flexible, and free-standing electrode comprising an unprecedented 92% silicon content. In the microscroll, carbon-coated silicon nanoparticles are anchored on conductive carbon nanotubes and subsequently confined in cellulose carbon rolls with enough internal voids to accommodate the volume expansion of silicon; thus, a uniform dispersion of silicon with high reactivity was achieved. This structure shows an ultrahigh electrode-specific capacity of 2700 mA h g⁻¹, excellent cycling stability under a high silicon content of 85% (>2000 mA h g⁻¹ after 300 cycles) and a commercial-level areal capacity (5.58 mA h cm⁻²). This strategy offers a new way to design electrodes with a high active material content for high performance batteries.

Received 14th August 2019,
Accepted 19th November 2019

DOI: 10.1039/c9ee02615k

rsc.li/ees

Broader context

To satisfy the growing energy demands for electric vehicles and portable electronics, silicon has been extensively developed as a promising anode material for next-generation Li-ion batteries. Tremendous efforts have been devoted to designing and modifying the material nanostructures for improving the electrochemical performance, and thus demonstrating the bright prospects of silicon anodes. However, energy storage technologies using silicon anodes still have some big obstacles to overcome on their way to commercialization. There is a big gap between the lab condition results and industrial requirements, especially in terms of the scale-up ability, nanostructure robustness, and actual available capacity at the electrode level. In this work, we designed a robust silicon electrode with an unprecedented 92% silicon content and unique microstructure by a simple, green, low-cost and scalable method, which aims to solve the above issues towards commercial application of silicon. Owing to the self-rolling of cellulose nanosheets in the synthetic process, Si nanoparticles are wrapped into binder-free flexible electrodes with controllable Si content. The designed microscroll electrodes with well-engineered and robust structure show high specific capacity and good cycling stability. The method of cellulose-based topological roll design can also be used for other materials and systems with a high active material content.

Introduction

The development of lithium-ion batteries (LIBs) with a reduced weight, higher capacity, and longer service life is considered to

be the most important strategy to address the critical needs of applications such as next-generation mobile electronics and electric vehicles.^{1–4} Silicon (Si) has received wide-spread attention as the most promising anode material for the next generation of LIBs because of its high theoretical specific capacity of 3579 mA h g⁻¹ (Li₁₅Si₄).^{5–9} However, challenges arise owing to the large change in volume (>300%) under operation and poor electrical conductivity of Si, which significantly restricts the stability and kinetic process of the electrodes. In fact, to maintain electrode integrity, the industry has had to use a relatively low amount of Si (<15% by mass) in commercial anodes. Such a low Si content severely weakens the capacity advantage of silicon materials at the electrode level. To address

^a School of Engineering, Zhejiang A&F University, Hangzhou 311300, China. E-mail: qfsun@zafu.edu.cn

^b State Key Laboratory of Materials Processing and Die & Mould Technology, School of Materials Science and Engineering, Huazhong University of Science and Technology (HUST), Wuhan 430074, China. E-mail: hqli@hust.edu.cn

^c Department of Materials Science and Engineering, Stanford University, Stanford, California 94305, USA. E-mail: yicui@stanford.edu

† Electronic supplementary information (ESI) available. See DOI: 10.1039/c9ee02615k

‡ These authors contributed equally to this work.

the volume expansion and conductivity problems, researchers have devoted a large amount of effort to developing porous nano-architectures and combining Si with conductive carbon.^{10–16} But these modifications still yield a low Si content (<70%) in the electrode and it remains challenging to reach the commercial level of active materials in electrodes, which is typically >95% for graphite anodes and >85% for $\text{Li}_4\text{Ti}_5\text{O}_{12}$ anodes. To achieve a high energy density electrode, it is necessary to increase the active material content in silicon electrodes while at the same time maintaining good electrochemical properties.

Pioneering studies found that the pulverization problem caused by the large lithiation/delithiation strains can be minimized when the silicon particles are smaller than a critical size (<~150 nm) and the electrode is well-constructed with interior void space or pre-formed porosity to buffer the volume change.^{17–21} Based on these findings, various nanostructured silicon-based materials have been designed, namely nanowires,^{22–24} nanotubes,²⁵ pomegranate structures,²⁶ yolk-shell structures,^{14,27} and porous spheres,^{28,29} as well as many others.^{13,30–36} Despite their significantly enhanced performance, most of these architectures have inadequate mechanical properties and are barely able to tolerate the high mechanical stresses during conventional electrode preparation processes (such as grinding, mixing, and roller pressing). However, because of the discontinuous structure, poor conductivity, and higher surface area of most types of nano-silicon, a large number of inactive components (namely conductive additives and binders; usually >30%) have to be used to construct a continuous, conductive network to disperse and fix these nanoparticles within the electrode. As a result, the electrode's silicon content is still relatively low in most academic studies, such as 56.4% in a yolk-shell structure Si/C electrode,¹⁴ 48% in a mesoporous silicon electrode,³⁷ 18% in a micron-sized porous Si/C sphere electrode,³⁸ and 7.5% in a Si/C-graphite electrode.¹² This low Si content results in the actual specific capacity calculated for the whole anode being far less than the theoretical capacity of silicon, let alone considering the unaccounted mass of the current collector in the electrode (>7 mg cm⁻² for copper foil), which prevents silicon anodes from providing the high energy density they are capable of providing. Furthermore, many of these porous architectures involve complex and costly material synthesis and processing procedures, such as chemical vapor deposition, metal-assisted chemical etching, and template-assisted processes, leading to limited scalability and hurdles to commercialization.^{25,39–41} So far, it is a big challenge to develop a low-cost and efficient way of achieving electrodes with a high silicon content, good stability, and excellent electrochemical properties.

In this study, we designed a cellulose-based topological microscroll structure to achieve an unprecedented silicon content of 92% without any binder for the entire electrode, and investigated the use of it as a flexible, binder-free, and self-standing anode for LIBs. Systematic experiments combined with theoretical calculations demonstrate that the silicon nanoparticles induce the cellulose nanosheets to roll up during a freeze-drying process, thus driving the Si nanoparticles (NPs) anchored on CNTs to embed into cellulose microscrolls (Si@CNT/Cel-microscrolls), in which the CNTs and Si NPs were wrapped into

the microscrolls along the axial direction. This design has multiple advantages: (i) the topological microscrolls formed through the cellulose nanosheets rolling themselves up effectively confine and fix the silicon nanoparticles in CNT/carbon cages, thereby achieving a high silicon load of up to 92% by mass of the whole electrode; (ii) the elastic CNTs/carbon network guarantee a good dispersion of the silicon nanoparticles and form internal void spaces within the microscroll, relieving the expansion stress of silicon and providing sufficient buffer space; (iii) the super-long and interconnected microscrolls (lengths >100 μm) using CNTs as a backbone enable a binder-free and free-standing flexible electrode with sufficient flexibility; and (iv) the synthesis method is simple, green, low-cost, and scalable. As a result, we have achieved a high electrode specific capacity (2704 mA h g⁻¹) with a high silicon content of up to 92%; this high silicon content means that the overall weight of the electrode is only about one-ninth that of a traditional graphite electrode. Moreover, this microscroll design provides a stable structure, good electrical conductivity, and adjustable electrode thickness, allowing it to exhibit high cycling stability under a high silicon content of 85% (>2000 mA h g⁻¹ after 300 cycles at 0.2 A g⁻¹), a high areal capacity (5.58 mA h cm⁻²), and a volumetric capacity of 930 mA h cm⁻³. The cellulose-based topological roll design can be applied to other materials to construct flexible electrodes with a high active material content.

Results and discussion

Fig. 1 shows a schematic of the Si@CNT/carbon microscroll (Si@CNT/C-microscroll) design along with scanning electron microscopy (SEM) and transmission electron microscopy (TEM) images. The designed microscroll has a continuous structure constructed from an axial arrangement of intertwined CNTs, in which well-dispersed silicon nanoparticles are anchored onto the CNTs. The exterior of the microscroll is wrapped by ultra-thin carbon derived from the pyrolysis of self-winding cellulose nanosheets. During the carbonization, a nanoscale carbon-coating layer is also formed on the surface of the Si NPs. Abundant void space exists in the interior of the microscroll and between the Si NPs, which can accommodate the volume expansion of silicon during the lithiation processes. The elastic CNT/C cages and the cellulose-derived carbon that are present throughout the scrolls, both internally and externally, help to create excellent conductive paths to the carbon-coated Si NPs and firmly support the silicon to prevent it from falling off the scroll. An SEM image of the synthesized Si@CNT/C-microscrolls shows a unique architecture that consists of ultra-long fibers (>100 μm in length) with a uniform geometry (Fig. 1b). Si NPs (30–50 nm) hang in bunched CNTs in a shape that resembles clusters of grapes (Fig. 1c). These bunched CNTs are strongly fixed to each other by cellulose-derived carbon, thus forming an intertwined, spiral CNT/carbon cage structure to steadily support the Si NPs. The microscrolls have plenty of voids, mainly in the meso/macroporous range from 10 to 100 nm (Fig. 1d and Fig. S1, ESI[†]). Fig. 1e shows a TEM image of one Si@CNT/C-microscroll with a well-constructed interior void

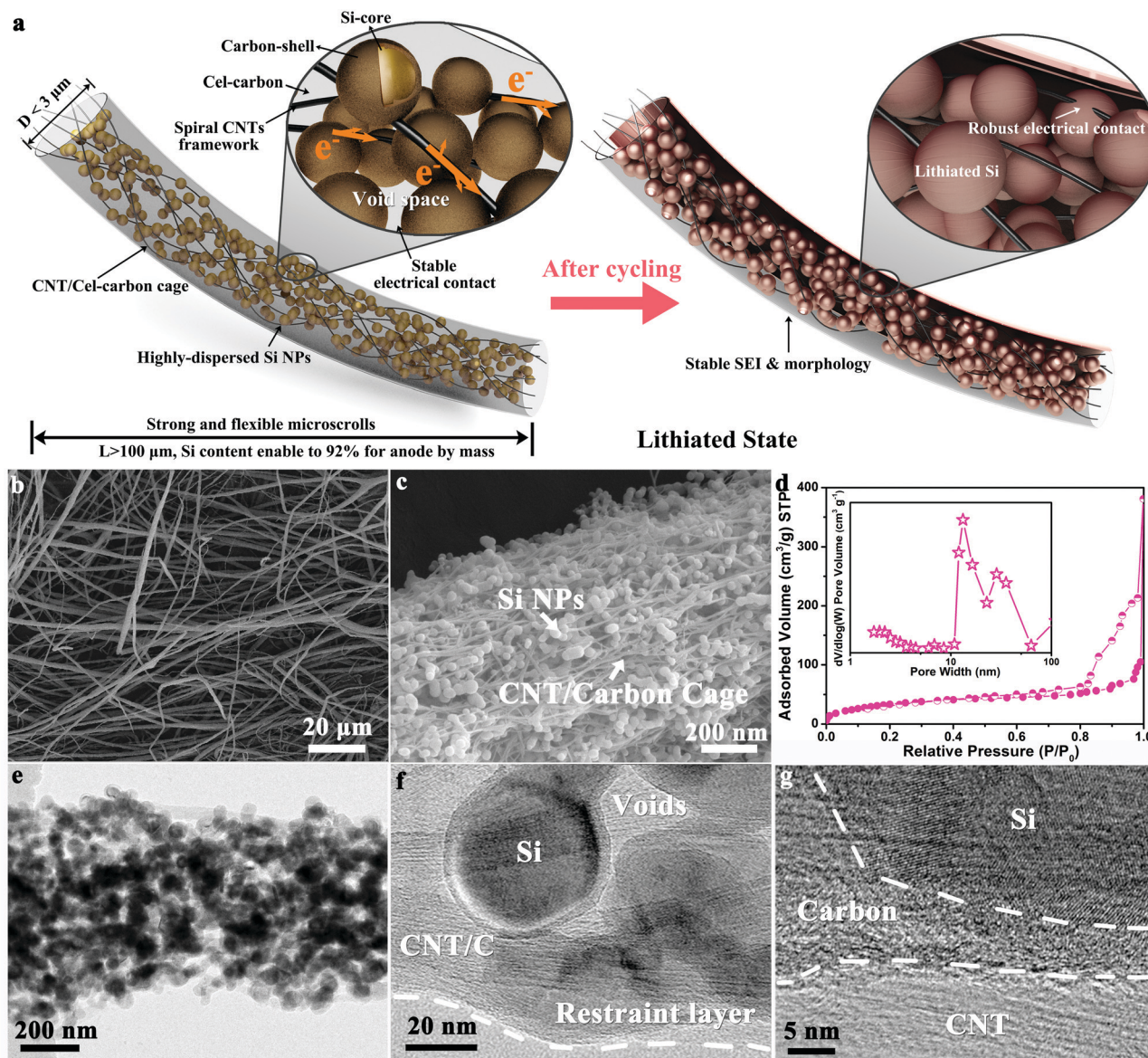


Fig. 1 Si@CNT/C-microscroll design. (a) One microscroll before and after electrochemical cycling. (b) SEM image of a Si@CNT/C-microscroll. (c) SEM image of one microscroll. (d) Nitrogen adsorption–desorption isotherm with a pore-size distribution curve of the Si@CNT/C-microscrolls showing good porosity (10–100 nm). (e and f) TEM and (g) HRTEM images of a Si@CNT/C-microscroll.

space in which Si NPs are well-dispersed without aggregation. Interestingly, the Si NPs are coated with a carbon nanolayer with a thickness of ~ 3 nm and possess stable electrical contacts with the CNTs (Fig. 1f, g and Fig. S2 and S3, ESI[†]), which should help enhance the activity and conductivity of the silicon.

In view of the above unique architecture in Fig. 1, we further explored the formation mechanism of the cellulose-based scrolls. Our approach for the preparation of Si@CNT/C-microscrolls involved ultrasonic treatment of a mixed solution of cellulose nanosheets (Fig. 2a), Si NPs (Fig. S4a, ESI[†]), and CNTs (Fig. S4b, ESI[†]) followed by freeze-drying and annealing. Cellulose, one of the main raw materials used here, has a unique two-dimensional laminate structure with a thickness of ~ 4 nm (Fig. S5, ESI[†]). It is worth noting that these cellulose nanosheets transform into the

microscrolls with a very high yield close to 100% after the freeze-drying process (Fig. 2b and c and Fig. S6, ESI[†]). Then, a series of comparative experiments were designed to determine the minimum necessary conditions for this transformation (Fig. S7–S9, ESI[†]). The results indicate that the occurrence of the topological transformation of the cellulose nanosheets depends on three main factors, namely the cellulose nanosheets, Si NPs, and the freeze-drying process. It is the freeze-drying process that creates the appropriate environment for the deformation of the cellulose nanosheets, such as by isolating the nanosheets to reduce the interactions between them and by providing a metastable solid/gas interface. Fig. S10 (ESI[†]) shows TEM images of the mixed solution of Si NPs and cellulose nanosheets before freeze-drying, where the cellulose nanosheet shows obvious characteristics of

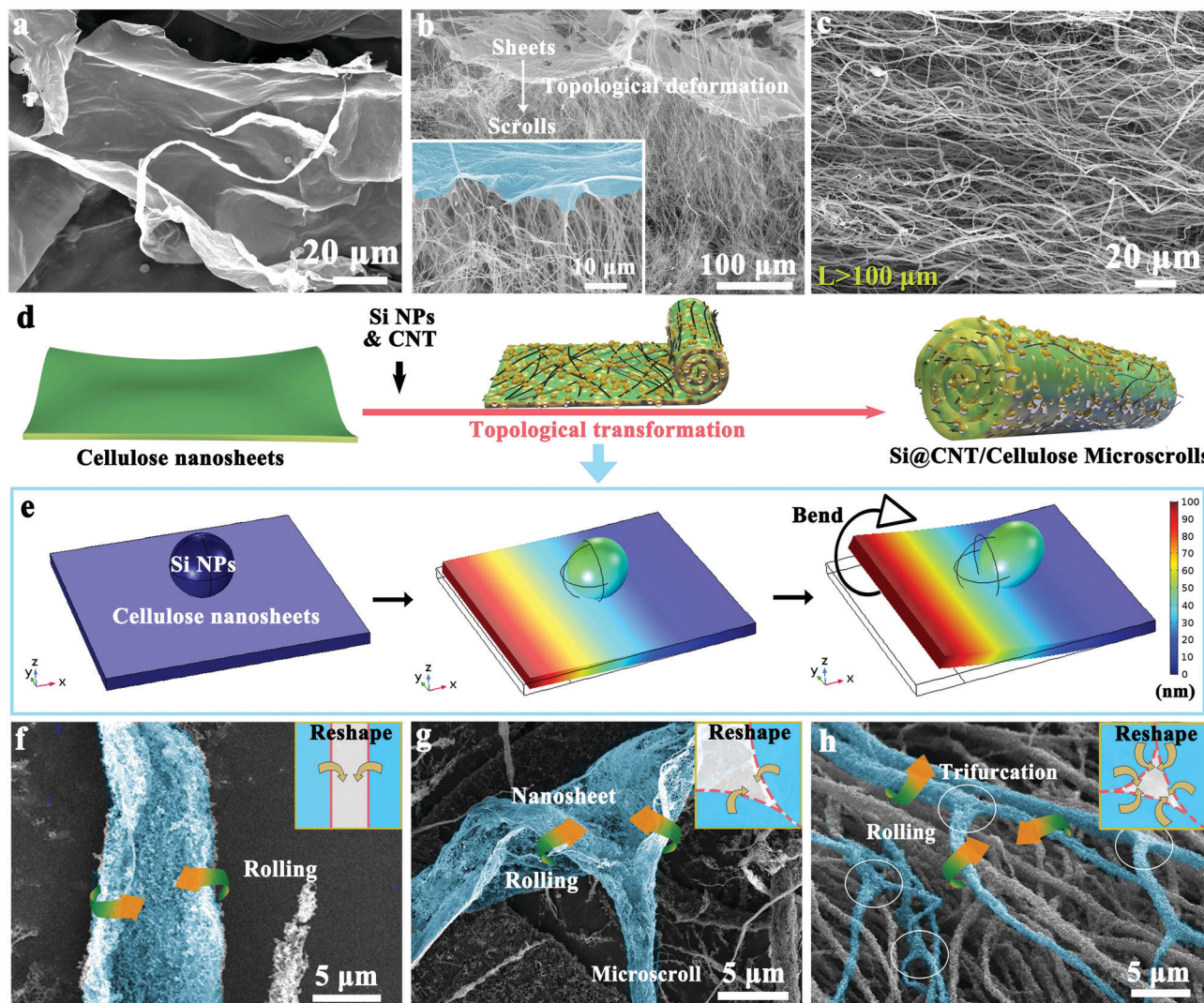


Fig. 2 Formation mechanism of Si@CNT/C-microscrolls. SEM images of (a) cellulose nanosheets, (b) the transition stage, which simultaneously shows the sheet and scroll structure, and (c) a Si@CNT/C-microscroll. The fibers in panel (b) were formed from the splitting and subsequent rolling up of nanosheets owing to the gaps observed between the fibers in their junction. (d) Corresponding schematic illustration of the topological deformation process for Si@CNT/C-microscrolls. (e) Simulation modeling of the topological deformation process of one side of a cellulose nanosheet with one Si NP. (f–h) SEM images of a Si@CNT/C-microscroll in the immediate state of topological deformation.

water swelling owing to ultrasonication. Generally, the dehydration treatment can cause shrinkage of cellulose in the presence of hydrogen bonds, which would be accompanied by a corresponding shrinkage stress.^{42,43} Therefore, we speculate that the rolling up of nanosheets is related to the stress caused by the Si NPs in an appropriate environment, *i.e.*, that provided by freeze-drying.

To understand the formation mechanism of the cellulose-based scrolls, we performed a simulation in which we model the topological deformation of a cellulose nanosheet (see Methods). In our model, the focus was elucidating the origin of the bending deformation of the cellulose nanosheet; the cellulose nanosheet was simplified into a laminar plate structure that can shrink in a vacuum. In this model, a silicon nanoparticle was placed on the surface of the nanosheet, thereby representing the initial state. The simulated snapshots of the topological deformation of the Si/cellulose nanosheets show a maximum displacement

of 90 nm in the Z direction (Fig. 2d, e and Fig. S11, Table S1, ESI[†]). The simulation results provide an important insight: the restraining action of the silicon nanoparticle can cause warping of the cellulose nanosheet during the dehydration/shrinkage process. When many Si NPs are placed on the nanosheet, this warping force may be even greater. In fact, we were also able to identify the transformation process in SEM images of samples in intermediate stages of the transformation process, as shown in Fig. 2f and g. The process is similar to how rolls of paper form, in the sense that all the edges of the nanosheets first curl up. As the rolling-up process starts simultaneously at multiple edges, abundant trifurcations are observed in the microscrolls, which benefit the construction of a high-speed conductive network (Fig. 2h). As a result, the presence of Si NPs causes a non-uniform shrinkage stress of the cellulose nanosheet during freeze-drying, inducing the cellulose nanosheet to roll itself up;

this process was verified both in our experiments and in our simulation.

Since each microscroll is self-assembled from Si NPs, cellulose nanosheets, and CNTs, we further regulated the ratio of each of these components, and observed that the microscroll structure could be obtained repeatedly over a wide range of different material mixing ratios (Fig. S12 and Table S2, ESI[†]). As shown in Fig. 3a, all the obtained samples show microscroll architectures for a CNT content between 1.8 and 21% and had similar structures to that shown in the magnified SEM images of a single scroll. Similarly, the microscroll structure was also well maintained for a Si content in the microscroll between 32 and 92% (Fig. 3b). Fig. 3c and d show a statistical analysis of the microscroll diameters for different amounts of CNTs and Si, indicating that when the content of the other two components was maintained at a certain proportion, the average diameters of the microscrolls could be increased by increasing the silicon content or by decreasing the CNT content; however, the diameter could not exceed 3 μm . This demonstrates that the change in content of either the silicon or CNTs only affected the average diameter of a microscroll, and that it did not have an influence on the formation of the microscrolls. The ability to achieve a wide range of material properties by adjusting the proportion of the components that make up the microscrolls provides the possibility to flexibly control the electrical conductivity and

specific capacity of the electrodes by increasing or decreasing their CNT and silicon content.

Based on this, it can be concluded that these unique microscroll architectures not only have flexibly adjustable functionalities, but also could also be mass manufactured owing to their synthesis route. As shown in Fig. 4a, our microscroll design satisfies the requirements for batch synthesis using cheap and readily-available cellulose as a raw material, which should allow for low-cost production of this material in large quantities. Owing to the high aspect ratio and abundant trifurcation, the microscrolls can form an integrated network structure in which the microscrolls are interlaced with each other in an aerogel. This structural feature enables the preparation of a free-standing electrode film without using any binder. By a simple compression process, an electrode membrane can be obtained without the need for traditional electrode processing methods such as mixing, coating, or solvent evaporation (Fig. 4b). Based on varying the amount of CNTs in the microscrolls, the conductivity of the electrodes can be adjusted from 31.6 to 421 S cm^{-1} (Fig. 4b and Fig. S13, ESI[†]). Even after compaction, bending, folding, and twisting, the free-standing electrode still maintains high flexibility with good integrity of the microscrolls (Fig. 4c, d and Fig. S14, ESI[†]), implying that this architecture has superior robustness compared with previously reported precise nanostructures^{26,31,44} such as hollow spheres and yolk-shell Si/C. The cross-sectional

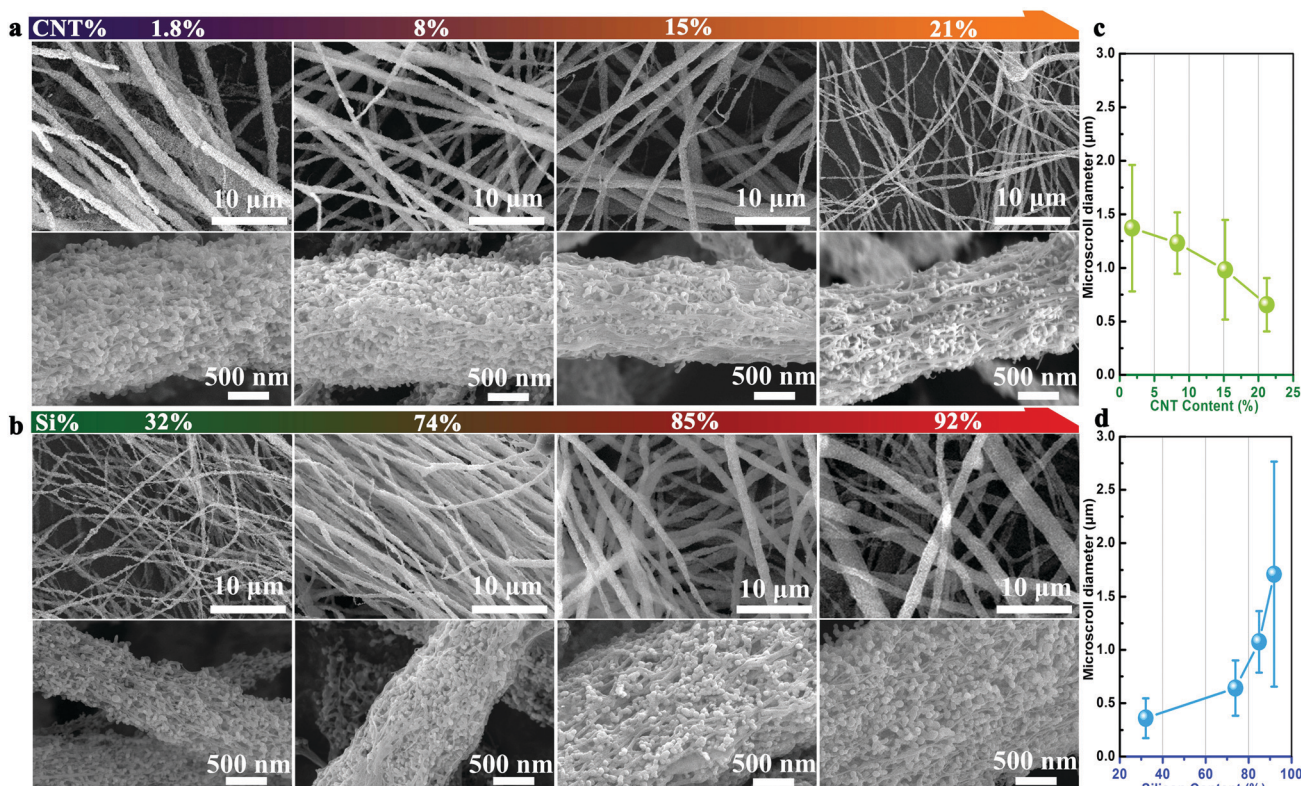


Fig. 3 Controllable synthesis of Si@CNT/C-microscrolls with varying concentrations of silicon and carbon. SEM images of Si@CNT/C-microscrolls with (a) a calculated CNT content and (b) a calculated silicon content of 32, 74, 85, and 92%. The lower half of the panel shows a single microscroll. The corresponding conditions are reported in Table S2 (ESI[†]). Panels (c) and (d) show the average diameters and the size distribution of the Si@CNT/C-microscrolls with different CNT and silicon content, respectively.

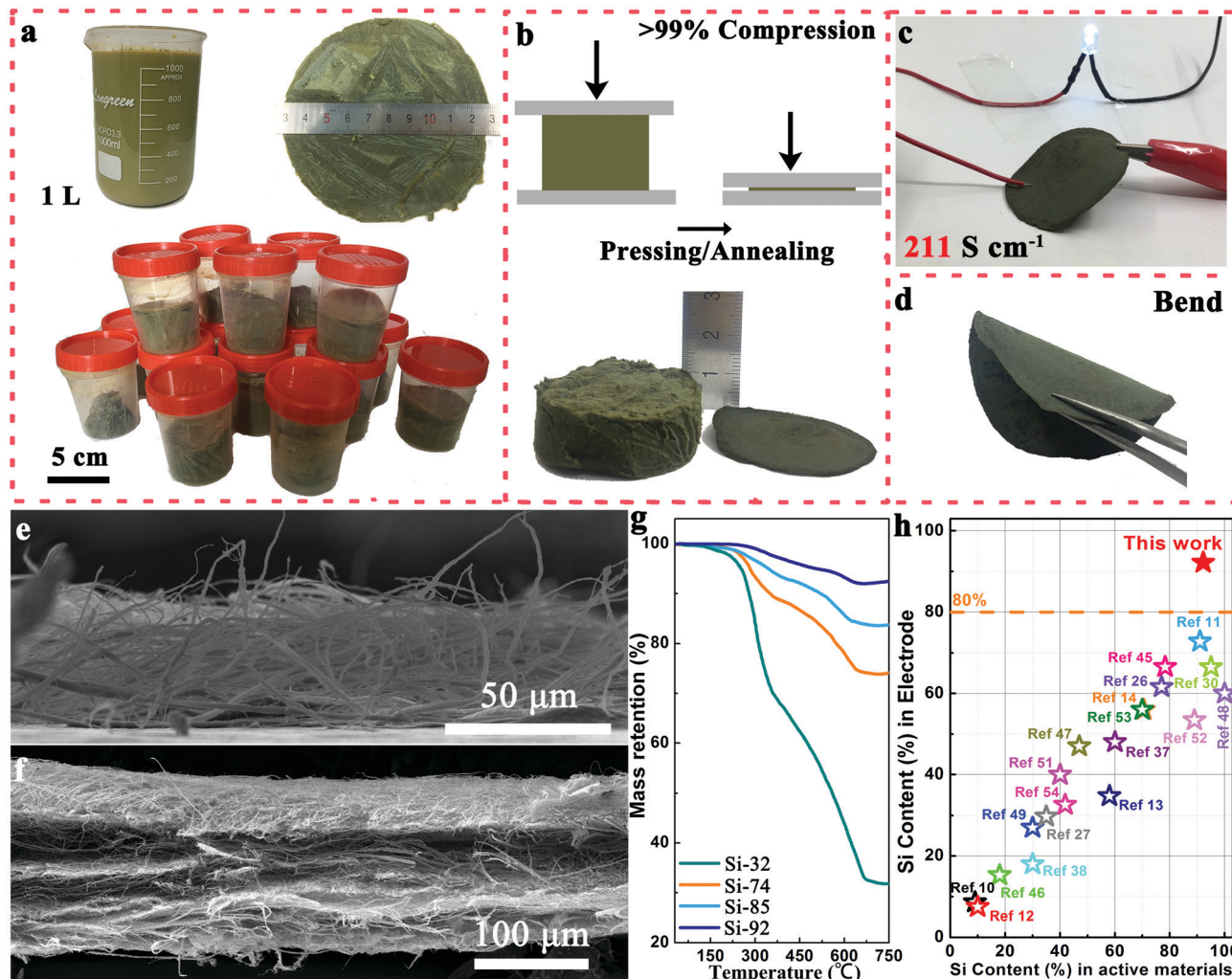


Fig. 4 Free-standing Si@CNT/C-microscroll electrode and its characteristics. Digital photographs of (a) 1 L of a Si@CNT/cellulose mixed solution along with the amount of Si@CNT/cellulose aerogel produced per batch; (b) a free-standing Si@CNT/C-microscroll electrode obtained through pressing and annealing the aerogel (>99% compression) with (c) excellent flexibility and (d) good conductivity (a Si content of 85%). Cross-sectional SEM images of a Si@CNT/C-microscroll electrode with a controllable mass of (e) 0.83 mg cm^{-2} or (f) 2.2 mg cm^{-2} . (g) Thermogravimetric curves of electrodes with a Si content of 31.2, 74.6, 84.5, and 92.2% (denoted as Si-32, 74, 85, and 92, respectively). (h) Comparison of the amount of Si content in the electrode; our work represents the maximum amount of silicon in an electrode compared with previously reported silicon/carbon anodes.

morphologies (Fig. 4e and f) of the free-standing electrodes show controllable loading and a stable microscroll structure. Additionally, thermogravimetric analysis was used to identify the actual silicon content of the free-standing Si@CNT/C-microscroll electrodes (a Si content of 31.2, 74.6, 84.5, and 92.2%, referred to as Si-32, 74, 85, and 92, respectively), which was in very good agreement with the theoretical values (Fig. 3b and 4g). It is important to note that even though no binders were used to fabricate the electrode, the topological scroll structure obtained by the rolling up of cellulose nanosheets allows the scrolls to tolerate a high silicon content of up to 92% while still maintaining a flexible electrode structure. To the best of our knowledge, this high Si content (compared with the entire mass of the electrode) is unprecedented based on our assessment of previously reported silicon/carbon anodes (Fig. 4h).^{10–14,26,27,30,37,38,45–54}

The unique microscroll design ensures remarkable battery performance. As shown in Fig. 5a, it is obvious that the

Si@CNT/C-microscroll electrode can operate with an ultrahigh silicon content of $\sim 92\%$. The electrode has a high initial discharge capacity of 3254 mA h g^{-1} at a current density of 0.2 A g^{-1} (the total weight of the electrode was taken into account in all these calculations), corresponding to an initial coulombic efficiency (ICE) of 83.6% (Fig. 5b). The irreversible capacity loss at the first cycle is mainly caused by the formation of SEI layers.⁵⁵ The electrode also had a good reversible capacity of 2704 mA h g^{-1} at 0.2 A g^{-1} (Fig. S15, ESI[†]), indicating that the topological microscroll design enables excellent utilization of the silicon through the continuous conductive network throughout the entire microscroll. The carbon content in the microscroll can affect the ICE, with the ICE decreasing from 83.6 to 76.4% when the carbon content was increased from 7.8 to 15.4% (Fig. 5b and Fig. S12, ESI[†]). A similar phenomenon has also been reported by Liu *et al.*²⁶ that lower carbon content in the composite corresponds to a higher first cycle ICE, primarily owing to less lithium trapping by the

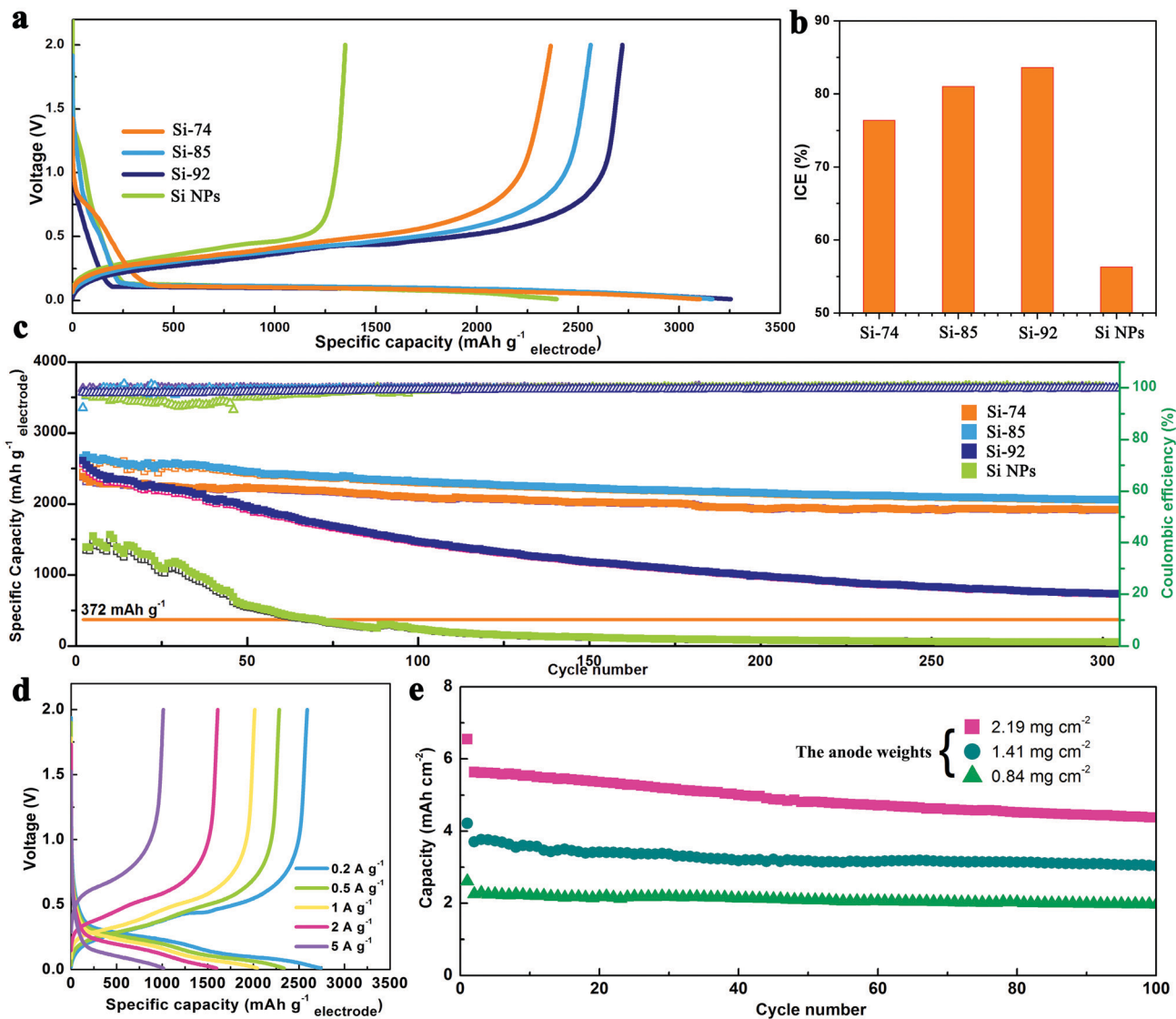


Fig. 5 Electrochemical performance of the Si@CNT/C-microscroll electrode. (a) First cycle of the discharge–charge voltage curves of the Si@CNT/C-microscroll electrode (for Si-74, 85, and 92) and for an electrode with 50% Si NPs (Si NP-50). If not otherwise stated, all reported capacities in all panels of this figure are based on the total mass of the whole of the electrode—this does not include the current collector for the Si NP-50 electrode. (b) Comparison of the initial coulombic efficiency. (c) Cyclability of the Si NP-50 electrode and the Si@CNT/C-microscroll electrode (Si-74, 85, and 92) at 0.2 A g^{-1} . (d) Voltage profiles of the Si-85 electrode cycled at various rates from 0.2 to 5 A g^{-1} in a potential window from 0.01 to 2 V versus Li/Li⁺. (e) Capacities at a slow rate of 0.2 A g^{-1} with anodes with different masses.

amorphous carbon. Compared with an ICE of 56.3% for an electrode with 50% Si NPs (Si NP anode), a higher ICE was achieved for the Si@CNT/C-microscroll electrode owing to the unique microscroll structure, which effectively encapsulates the Si NPs inside the scroll and forms a carbon coating layer on the silicon surface. Fig. 5c demonstrates the prolonged cycling performance of Si@CNT/C-microscroll electrodes for 300 cycles. With a silicon content of 84.5% (Si-85), the Si@CNT/C-microscroll electrode was able to maintain outstanding cycling stability, delivering a stable capacity of 2056 mA h g^{-1} after 300 cycles, in comparison with 54.6 and 1913 mA h g^{-1} for the pure Si electrode and the Si-74 electrode, respectively. This demonstrates that the microscrolls have a superior structural design as they can remain stable under cycling even without binder and with a high

Si content. For the Si-92 anode, with a silicon content as high as 92%, the microscroll electrode still showed a high reversible capacity of 732 mA h g^{-1} after 300 cycles, over two times the capacity of graphite (372 mA h g^{-1}).

As shown in Fig. 5d and Fig. S16 (ESI[†]), rate performance tests of the Si@CNT/C-microscroll and Si NP electrodes were conducted at various rates between 0.2 and 5 A g^{-1} . The Si@CNT/C-microscroll electrode has a good rate capability because of its good kinetics, which is in part synergistically derived from the scroll-packaged and carbon-coated Si NPs and the conductive CNT/C framework. Discharge capacities of 2710, 2320, 2085, 1611, and 1016 mA h g^{-1} were obtained at 0.2, 0.5, 1, 2, and 5 A g^{-1} , respectively; these capacities are much higher than the capacities of the Si NP electrode, which ranged from

1543 to 20 mA h g⁻¹. After cycling at a high rate and returning the current density back to 0.5 A g⁻¹, a stable capacity of 2154 mA h g⁻¹ was restored. We can thus conclude that the topological microscroll structure of the Si@CNT/C-microscroll electrode, including the encapsulation and fixation of the Si NPs in the porous interior of the scroll and the stable electrical contact with elastic CNT/C cages, significantly improves the cycle performance.

Achieving a high areal capacity with a low electrode weight is a key requirement for light, high-energy density batteries (Fig. 5e). The areal capacity of the microscroll electrodes was able to reach 5.58 mA h cm⁻² (2548 mA h g⁻¹) with a mass loading of 2.19 mg cm⁻² at 0.2 A g⁻¹ and was able to maintain good stability (>78% after 100 cycles). The corresponding volumetric capacity based on the electrode volume was determined to be 930 and 720 mA h cm⁻³ (thickness: ~60 μm; density: 0.365 g cm⁻³) before and after cycling, respectively, higher than the 600 mA h cm⁻³ achieved by graphite anodes. More importantly, the overall weight of the electrode was only about one-ninth that of a traditional graphite electrode with a similar areal capacity. The electrode can maintain a good areal specific capacity under a higher silicon loading with a thicker electrode condition, owing to the integration of the electrode and unique microscroll structure. The integrated microscrolls

effectively prevent electrode cracking during repeated cycling even for a thicker electrode, in which the Si NPs can be well fixed within the microscrolls.⁵⁶ The areal and specific capacities of this free-standing electrode outperform those of most previously reported Si-based electrodes (Fig. S17 and Table S3, ESI†). Besides, by using this Si microscroll electrode as the anode and LiFePO₄ as the cathode, a LiFePO₄/Si full cell was successfully constructed (Fig. S18, ESI†). The full cell exhibits a good gravimetric discharge capacity of 2636 mA h g⁻¹ at 0.3C. When the cell was bent, it can work well to light an LED, demonstrating that such a flexible microscroll electrode also provides good electrochemical performance in a full battery.

To demonstrate the robustness of this unique microscroll structured electrode, the change in the morphology of the Si@CNT/C-microscroll and Si NP electrodes after cycling was also investigated, as shown in Fig. 6. After discharging/charging at 0.2 A g⁻¹ for 50 cycles, obvious cracks were observed in the surface of the Si NP electrode (Fig. 6a). Additionally, severe pulverization, aggregation, and desquamation occurred in the Si NPs. In contrast, the topological microscrolls of the Si@CNT/C-microscroll electrode exhibited good structural stability. No cracks or fractures were observed in the surface of the microscrolls (Fig. 6b), suggesting that these topological microscrolls are stable enough to withstand the significant volume changes

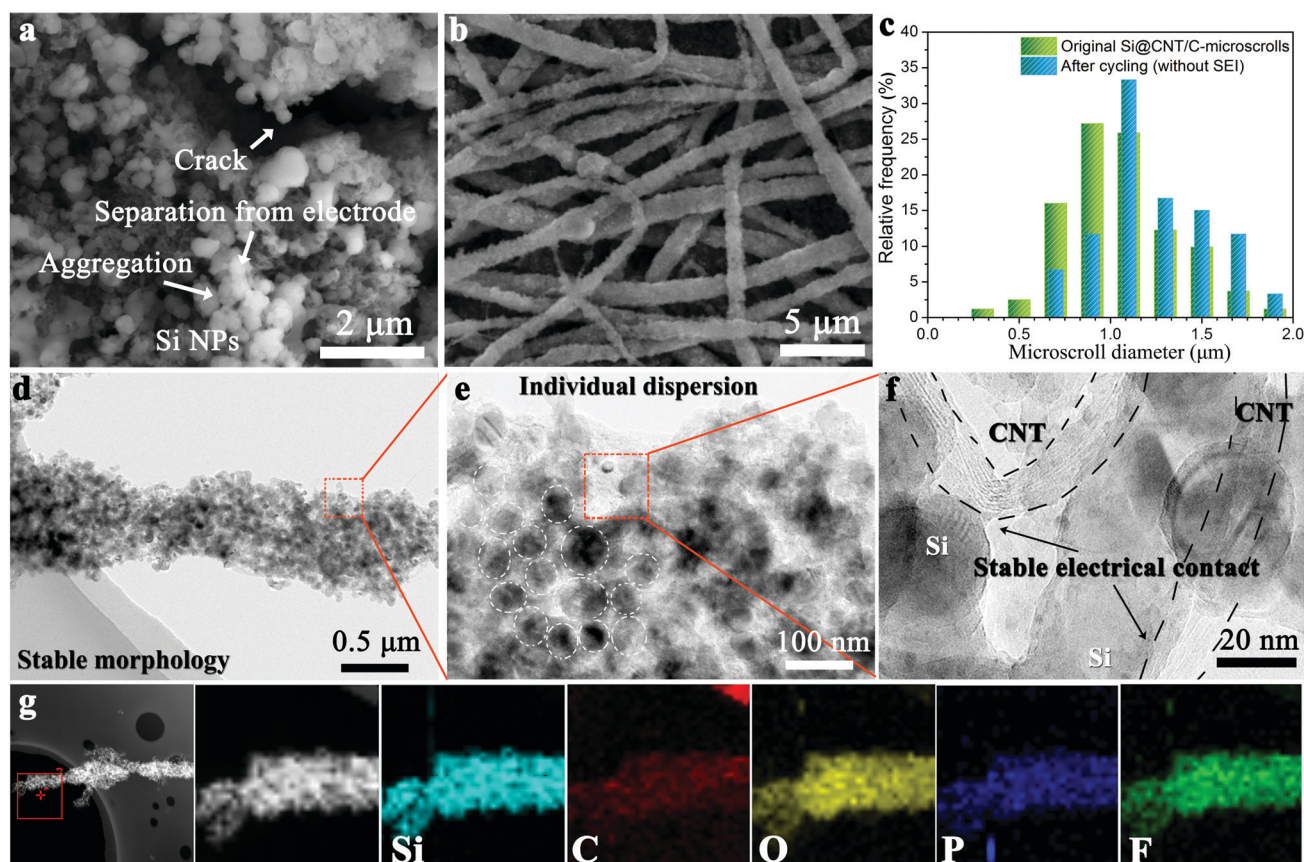


Fig. 6 Morphological evolution of the electrode after the lithiation/delithiation processes. SEM image of (a) the Si NP electrode and (b) the Si@CNT/C-microscroll electrode without the SEI. (c) Statistical analysis of the diameters of the microscrolls before and after cycling. (d–f) TEM image and high-resolution images of the electrode after cycling, and (g) corresponding Si, C, O, P, and F elemental maps.

of Si during the lithiation/delithiation processes. A statistical analysis shows a slight increase of the microscroll diameters after cycling (Fig. 6c). The average diameter of the microscrolls was 15% larger after cycling, increasing from 1.04 to 1.20 μm , demonstrating that the microscroll design has an excellent tolerance for silicon's expansion. TEM images with elemental mapping results for a Si@CNT/C-microscroll are shown in Fig. 6d and e. The microscroll clearly shows a stable morphology in which the Si NPs are individually dispersed in the scroll without aggregating, and a large amount of voids remain between the nanoparticles. Additionally, these nanoparticles are still fixed to the CNTs and thus maintain good electrical contact with the CNT/C framework even after cycling (Fig. 6f). As a result, the above factors collectively contribute to mitigating the volume expansion and to maintaining the good electrochemical activity of silicon, thereby enhancing the cycling stability of the flexible and free-standing microscroll electrodes.

Conclusions

In summary, we have designed a new microscroll structure to successfully address the issue of low silicon content in silicon electrodes and have realized an unprecedented silicon content of 92% for the whole flexible and self-supporting electrode. We have demonstrated that the unique microscroll architecture is related to the topological deformation of cellulose nanosheets in the presence of Si NPs under freeze-drying. This microscroll architecture also has the possibility to flexibly adjust the functional components as well as having the potential to be produced in large quantities at low-cost. The unique microscroll design has multiple favorable properties that enable the superior electrochemical performance of the Si@CNT/C-microscroll electrode: well-fixed and highly dispersed Si NPs, interior voids, a coating of cellulose carbon around the whole scroll, and highly conductive and elastic CNT/C cages. The electrode containing a high silicon content of 85% can well deliver a large capacity of 2710 mA h g^{-1} at 0.2 A g^{-1} with good cycling stability. This work demonstrates a new, green strategy for electrode design with a high loading content of active material.

Experimental

Synthesis

As illustrated in Fig. 2d, mixes of cellulose nanosheets,^{57–59} CNTs, and commercial silicon nanoparticles in certain weight proportions (Table S1, ESI[†]) were uniformly dispersed in 1 L of deionized water using ultrasonication for 15 min before they were transferred to different containers to control the loading of silicon (Fig. 4a). After a simple freeze-drying treatment, the resultant homogeneous yellow solution was converted into an aerogel composed of Si@CNT/cellulose microscrolls. To enhance the throughput per batch during the annealing process, the aerogels were pressed (for later slicing) using a pressure of 5 MPa. Finally, compacted Si@CNT/C-microscrolls were synthesized after annealing at 800 $^{\circ}\text{C}$ for 2 h. The structure of the

silicon remained consistent from the start to the end of the process (Fig. S19, ESI[†]). Based on the mass percentage of Si in the final microscrolls, the samples were named Si-*X* (where *X* is the silicon content [%]). For example, Si-32 represents a silicon content of 32% in the microscroll and free-standing electrode. Additionally, Si@CNT/Cel-microscroll was synthesized as an intermediate state during the topological transformation by scraping the surface of the partially freeze-dried sample followed by drying in an oven at 60 $^{\circ}\text{C}$.

Mechanical modelling

We only considered one silicon particle for the modeling, and simplified the cellulose nanosheets into a laminar plate structure. The diameter of the silicon particle was 50 nm, and the size of cellulose nanosheet was 200 nm \times 200 nm \times 10 nm. During the freeze-drying process, the swollen cellulose nanosheets shrank owing to the loss of water. Our model mainly focused on the deformation of the cellulose nanosheets during the contraction process for the case of a silicon nanoparticle placed on the nanosheet's surface. To simulate the boundary of the nanosheet, this work only considered one possible shrinking process: only one side was shrunk in the *X* direction. Herein, the bottom of the cellulose nanosheet was fixed. It was assumed that the nanosheet would shrink along the *X* direction, and the *Y* direction has a normal constraint. The detailed setup of the model and the material parameters is described in the ESI[†].

Electrochemistry

The battery performance was evaluated by galvanostatic cycling of coin cells with free-standing Si@CNT/C-microscrolls as the working electrode and lithium foil as the counter and reference electrode. The mass loading of the whole anode (Si-85) ranged from 0.8 to 2.4 mg cm^{-2} . Control electrodes with Si NPs were prepared using the common slurry method, except using a mass ratio of 5 : 3 : 2 for the active material, Super-P, and PVDF; this electrode is referred to as Si NPs. After casting onto Cu foil and drying at 60 $^{\circ}\text{C}$ in an oven for 12 h, a pure Si anode was prepared with a mass loading of $\sim 0.8 \text{ mg cm}^{-2}$. To assess the electrochemical performance of microscrolls with a different Si content, the Si-74 and Si-92 electrodes were tested with a mass loading of 0.8–1 mg for the whole of the anodes. The electrolyte was 1 M LiPF_6 in 3 : 6 : 1 v/v/v ethylene carbonate/diethyl carbonate/fluoroethylene carbonate. All the cells were cycled between 0.01 and 2 V *versus* Li/Li^+ .

Conflicts of interest

There are no conflicts to declare.

Acknowledgements

The work was supported by Zhejiang Provincial Natural Science Foundation for Distinguished Young Scholars of China under Grant No. LR19C160001; the National Natural Science Foundation of China (51772115, 21571073), Hubei Provincial Natural Science

Foundation of China (2019CFA002), and the Fundamental Research Funds for the Central University (2019kfyXMBZ018). The authors also thank the Analytical and Testing Center of HUST for the measurements.

Notes and references

- J. M. Tarascon and M. Armand, *Nature*, 2001, **414**, 359–367.
- D. Bruce, K. Haresh and T. Jean-Marie, *Science*, 2011, **334**, 928–935.
- J. W. Choi and D. Aurbach, *Nat. Rev. Mater.*, 2016, **1**, 16013.
- S. Chu, Y. Cui and N. Liu, *Nat. Mater.*, 2016, **16**, 16.
- H. Wu and Y. Cui, *Nano Today*, 2012, **7**, 414–429.
- M. N. Obrovac and V. L. Chevrier, *Chem. Rev.*, 2014, **114**, 11444–11502.
- S. Choi and G. Wang, *Adv. Mater. Technol.*, 2018, **3**, 1700376.
- S. Choi, T.-w. Kwon, A. Coskun and J. W. Choi, *Science*, 2017, **357**, 279–283.
- Y. Jin, B. Zhu, Z. Lu, N. Liu and J. Zhu, *Adv. Energy Mater.*, 2017, **7**, 1700715.
- M. Ko, S. Chae, J. Ma, N. Kim, H. W. Lee, Y. Cui and J. Cho, *Nat. Energy*, 2016, **1**, 16113.
- Y. Li, Y. Kai, H. W. Lee, Z. Lu, N. Liu and C. Yi, *Nat. Energy*, 2016, **1**, 15029.
- X. Li, P. Yan, X. Xiao, J. H. Woo, C. Wang, J. Liu and J.-G. Zhang, *Energy Environ. Sci.*, 2017, **10**, 1427–1434.
- Y. Han, J. Zou, Z. Li, W. Wang, Y. Jie, J. Ma, B. Tang, Q. Zhang, X. Cao, S. Xu and Z. L. Wang, *ACS Nano*, 2018, **12**, 4835–4843.
- S. Chen, L. Shen, P. A. van Aken, J. Maier and Y. Yu, *Adv. Mater.*, 2017, **29**, 1605650.
- C.-F. Sun, H. Zhu, M. Okada, K. Gaskell, Y. Inoue, L. Hu and Y. Wang, *Nano Lett.*, 2015, **15**, 703–708.
- W. J. Lee, T. H. Hwang, J. O. Hwang, H. W. Kim, J. Lim, H. Y. Jeong, J. Shim, T. H. Han, J. Y. Kim, J. W. Choi and S. O. Kim, *Energy Environ. Sci.*, 2014, **7**, 621–626.
- C. K. Chan, H. Peng, L. Gao, K. Mcilwrath, F. Z. Xiao, R. A. Huggins and Y. I. Cui, *Nat. Nanotechnol.*, 2008, **3**, 31.
- L. Y. Beaulieu, K. W. Eberman, R. L. Turner, L. J. Krause and J. R. Dahn, *Electrochem. Solid-State Lett.*, 2001, **4**, A137.
- T. D. Hatchard and J. R. Dahn, *J. Electrochem. Soc.*, 2004, **151**, A838–A842.
- X. Lai, J. E. Halpert and D. Wang, *Energy Environ. Sci.*, 2012, **5**, 5604–5618.
- B. Ding, H. Wu, Z. Xu, X. Li and H. Gao, *Nano Energy*, 2017, **38**, 486–493.
- C. Yu, L. Liu, X. Jie, T. Yang, Q. Yong and C. Yan, *Adv. Funct. Mater.*, 2016, **25**, 6701–6709.
- J. Wan, A. F. Kaplan, J. Zheng, X. Han, Y. Chen, N. J. Weadock, N. Faenza, S. Lacey, T. Li, J. Guo and L. Hu, *J. Mater. Chem. A*, 2014, **2**, 6051–6057.
- T. Song, L. Hu and U. Paik, *J. Phys. Chem. Lett.*, 2014, **5**, 720–731.
- H. Wu, G. Chan, J. W. Choi, I. Ryu, Y. Yao, M. T. Mcdowell, S. W. Lee, A. Jackson, Y. Yang and L. Hu, *Nat. Nanotechnol.*, 2012, **7**, 310–315.
- L. Nian, L. Zhenda, Z. Jie, M. T. Mcdowell, L. Hyun-Wook, Z. Wenting and C. Yi, *Nat. Nanotechnol.*, 2014, **9**, 187–192.
- H. Su, A. A. Barragan, L. Geng, D. Long, L. Ling, K. N. Bozhilov, L. Mangolini and J. Guo, *Angew. Chem., Int. Ed.*, 2017, **56**, 10780–10785.
- Q. Xiao, M. Gu, H. Yang, B. Li, C. Zhang, Y. Liu, F. Liu, F. Dai, L. Yang and Z. Liu, *Nat. Commun.*, 2015, **6**, 8844.
- S. Chen, P. Bao, X. Huang, B. Sun and G. Wang, *Nano Res.*, 2014, **7**, 85–94.
- C. Shen, X. Fang, M. Ge, A. Zhang, Y. Liu, Y. Ma, M. Mecklenburg, X. Nie and C. Zhou, *ACS Nano*, 2018, **12**, 6280–6291.
- D. Lin, Z. Lu, P.-C. Hsu, H. R. Lee, N. Liu, J. Zhao, H. Wang, C. Liu and Y. Cui, *Energy Environ. Sci.*, 2015, **8**, 2371–2376.
- X. Xie, K. Kretschmer, J. Zhang, B. Sun, D. Su and G. Wang, *Nano Energy*, 2015, **13**, 208–217.
- Y. Jiang, Y. Li, W. Sun, W. Huang, J. Liu, B. Xu, C. Jin, T. Ma, C. Wu and M. Yan, *Energy Environ. Sci.*, 2015, **8**, 1471–1479.
- Y. Jiang, Y. Li, P. Zhou, Z. Lan, Y. Lu, C. Wu and M. Yan, *Adv. Mater.*, 2017, **29**, 1606499.
- W. Wen, J.-M. Wu, Y.-Z. Jiang, L.-L. Lai and J. Song, *Chem*, 2017, **2**, 404–416.
- J. Lang, B. Ding, S. Zhang, H. Su, B. Ge, L. Qi, H. Gao, X. Li, Q. Li and H. Wu, *Adv. Mater.*, 2017, **29**, 1701777.
- N. Kim, H. Park, N. Yoon and J. K. Lee, *ACS Nano*, 2018, **12**, 3853–3864.
- M.-G. Jeong, H. L. Du, M. Islam, J. K. Lee, Y.-K. Sun and H.-G. Jung, *Nano Lett.*, 2017, **17**, 5600–5606.
- R. V. Salvatierra, A. R. O. Raji, S. K. Lee, Y. Ji and J. M. Tour, *Adv. Energy Mater.*, 2016, **6**, 1600918.
- X. Zhang, X. Qiu, D. Kong, L. Zhou, Z. Li, X. Li and L. Zhi, *ACS Nano*, 2017, **11**, 7476–7484.
- Z. Xiaosi, W. Li-Jun and G. Yu-Guo, *Small*, 2013, **9**, 2684–2688.
- H. Jin, Y. Nishiyama, M. Wada and S. Kuga, *Colloids Surf., A*, 2004, **240**, 63–67.
- L. Falk, H. Emmerich, W. Martin, N. Marie-Alexandra, S. Kerstin, M. Peter, H. Thomas, P. Antje and R. Thomas, *Macromol. Biosci.*, 2010, **10**, 349–352.
- N. Liu, H. Wu, M. T. Mcdowell, Y. Yao, C. Wang and Y. Cui, *Nano Lett.*, 2012, **12**, 3315.
- F.-H. Du, Y. Ni, Y. Wang, D. Wang, Q. Ge, S. Chen and H. Y. Yang, *ACS Nano*, 2017, **11**, 8628–8635.
- D. Vrankovic, M. Graczyk-Zajac, C. Kalcher, J. Rohrer, M. Becker, C. Stabler, G. Trykowski, K. Albe and R. Riedel, *ACS Nano*, 2017, **11**, 11409–11416.
- J. Zhu, T. Wang, F. Fan, L. Mei and B. Lu, *ACS Nano*, 2016, **10**, 8243–8251.
- M. Sohn, D. G. Lee, H.-I. Park, C. Park, J.-H. Choi and H. Kim, *Adv. Funct. Mater.*, 2018, **28**, 1800855.
- Q. Xu, J.-K. Sun, Y.-X. Yin and Y.-G. Guo, *Adv. Funct. Mater.*, 2018, **28**, 1705235.
- Y. Liu, Z. Tai, T. Zhou, V. Sencadas, J. Zhang, L. Zhang, K. Konstantinov, Z. Guo and H. K. Liu, *Adv. Mater.*, 2017, **29**, 1703028.
- H. Shang, Z. Zuo, L. Yu, F. Wang, F. He and Y. Li, *Adv. Mater.*, 2018, **30**, 1801459.

- 52 J. Yang, Y. Wang, W. Li, L. Wang, Y. Fan, W. Jiang, W. Luo, Y. Wang, B. Kong, C. Selomulya, H. K. Liu, S. X. Dou and D. Zhao, *Adv. Mater.*, 2017, **29**, 1700523.
- 53 S. Chae, M. Ko, S. Park, N. Kim, J. Ma and J. Cho, *Energy Environ. Sci.*, 2016, **9**, 1251–1257.
- 54 L. David, R. Bhandavat, U. Barrera and G. Singh, *Nat. Commun.*, 2016, **7**, 10998.
- 55 B. Gattu, R. Epur, M. Datta, A. Manivannan and P. Kumta, *Electrochem. Soc.*, 2014, **137**, 145.
- 56 S.-H. Park, P. J. King, R. Tian, C. S. Boland, J. Coelho, C. Zhang, P. McBean, N. McEvoy, M. P. Kremer, D. Daly, J. N. Coleman and V. Nicolosi, *Nat. Energy*, 2019, **4**, 560–567.
- 57 L. Yun, Q. Sun, D. Yang, X. She, X. Yao, G. Zhu, Y. Liu, H. Zhao and L. Jian, *J. Mater. Chem.*, 2012, **22**, 13548–13557.
- 58 H. Wang, L. Hu, C. Wang, Q. Sun, H. Li and T. Zhai, *J. Mater. Chem. A*, 2019, **7**, 3632–3641.
- 59 Q. Yao, Y. Xiong, H. Wang, C. Wang and Q. Sun, *J. Mater. Chem. A*, 2017, **5**, 9580–9590.